Title
Improving Signal to Noise in Labeled Biological Specimens Using Energy-Filtered TEM of Sections with a Drift Correction Strategy and a Direct Detection Device

Permalink
https://escholarship.org/uc/item/2mj1h18v

Journal
Microscopy and Microanalysis, 20(3)

ISSN
1431-9276

Authors
Ramachandra, Ranjan
Bouwer, James C
Mackey, Mason R
et al.

Publication Date
2014-06-01

DOI
10.1017/s1431927614000452

Peer reviewed

Improving Signal to Noise in Labeled Biological Specimens using Energy-Filtered TEM of sections with a Drift Correction Strategy and a Direct Detection Device

Ranjan Ramachandra[*],[+], **James C. Bouwer**[*], **Mason R. Mackey**[*], **Eric Bushong**[*], **Steven T. Peltier**[*], **Nguyen-Huu Xuong**[*], and **Mark H. Ellisman**[*]

[*]Center for Research in Biological Systems, National Center for Microscopy and Imaging Research, University of California at San Diego, 9500 Gilman Dr., La Jolla, CA 92093, USA

Abstract

Energy filtered transmission electron microscopy techniques are regularly used to build elemental maps of spatially distributed nanoparticles in materials and biological specimens. When working with thick biological sections, EELS techniques involving core-loss electrons often require exposures exceeding several minutes to provide sufficient signal to noise. Image quality with these long exposures is often compromised by specimen drift, which results in blurring and reduced resolution. To mitigate drift artifacts, a series of short exposure images can be acquired, aligned, and merged to form a single image. For samples where the target elements have extremely low signal yields, the use of CCD based detectors for this purpose can be problematic. At short acquisition times, the images produced by CCDs can be noisy and may contain fixed pattern artifacts that impact subsequent correlative alignment. Here we report on the use of direct electron detection devices (DDD's) to increase the signal to noise as compared to CCD's. A 3x improvement in signal is reported with a DDD vs. a comparably formatted CCD, with equivalent dose on each detector. With the fast rolling-readout design of the DDD, the duty cycle provides a major benefit, as there is no dead time between successive frames.

Keywords

EFTEM; direct detection device; DDD; CCD; DE-12; drift correction; endosomes; astrocytes

Introduction

Elemental maps of spatially distributed nanoparticles and sub-nanometer sized particles are regularly obtained using both Spectrum-Imaging in STEM (Scanning Transmission Electron Microscopy) and EFTEM (Energy Filtered Transmission Electron Microscopy) methods (Browning, et al., 1997; Grogger, et al., 2005; Leapman, 2003; Lozano-Perez, et al., 2009; Suenaga, et al., 2009). The most popular method for constructing EFTEM images is the collection of electrons that have lost a specific amount of energy due to an inner-shell ionization event with the atoms of the sample. These are generally referred to as core-loss or

[+]Corresponding author: raramachandra@ucsd.edu, Phone Number: 858-534-0276.

high-loss images (Egerton, 1996). Elemental mapping with electron energy loss spectroscopy (EELS), generally has better energy resolution, spatial resolution and minimum detection limits in comparison to traditional X-ray energy dispersive spectroscopy (XEDS) (Carter & Williams, 2009). Many recent studies have used electron energy loss techniques to explore applications in the biological sciences to detect calcium, iron and phosphorus in cells and tissues (Aronova, et al., 2008; Aronova, et al., 2009; Leapman & Aronova, 2007; Zhang, et al., 2005). However, for heavy elements, commonly used for labeling of biological specimens, the core-loss signal is an extremely small fraction of the background intensity (Egerton, 1996). In order to obtain EFTEM images to localize labels in biological specimens with sufficient signal-to-noise ratio (SNR), core loss EFTEM images generally require exposure times exceeding several minutes (Aoyama, et al., 2002). Such, long exposures invariably lead to deterioration in image quality, primarily due to specimen drift (Heil & Kohl, 2010; Hunt & Williams, 1991). A more efficient alternative to long exposure EFTEM imaging is to take a series of short exposure time images, and use drift correction to subsequently align and merge these individual images to form a single image (Aoyama, et al., 2002; Heil & Kohl, 2010; Schaffer, et al., 2004; Terada, et al., 2001). Such a strategy is known to reduce image blurriness and bring moderate improvements in the image resolution relative the conventional long exposure acquisition (Aoyama, et al., 2002; Heil & Kohl, 2010). However, this strategy brings only marginal improvement in the SNR quality of the image, and still requires the resolution-limiting step of on-chip image binning to boost the SNR (Aronova, et al., 2009; Heil, et al., 2012; Heil & Kohl, 2010; Hofer, et al., 1997).

Currently, most EFTEM imaging is performed using CCD based camera systems. In this paper, we describe the use of a new CMOS-based direct detection system, originally developed in our laboratory and now improved and commercially available as the DE12 from Direct Electron, LP. (Jin, et al., 2008; Milazzo, et al., 2009; Milazzo, et al., 2005; Milazzo, et al., 2010; Xuong, et al., 2007; Xuong, et al., 2004). Nearly 30 years ago, Egerton showed the inherent advantages of direct electron detection for EELS analysis, employing a conventional photo diode array (PDA) (Egerton, 1984). PDAs are generally built to detect photons, and direct exposure to high-energy electrons caused severe damage to the detector. As a result, not much progress had been reported on direct detection until our laboratory published on the new devices. (Egerton, 1996; Milazzo, et al., 2005). The direct electron detectors are beam-hardened CMOS devices able to withstand months of operation on a 300 KV TEM with out any significant beam damage (Jin, et al., 2008). Here, we show for the first time a significant increase in the SNR as compared to CCD detectors for energy-filtered imaging. The improved SNR with DDD detectors facilitates the recording of EFTEM images without any binning. In addition, the faster readout speed of the DDD detector and lack of dead time between successive frames reduces the acquisition time to create the resultant drift corrected EFTEM, making the direct detection device the ideal detector to improve SNR and image quality for drift corrected energy filtered imaging applications which, with a new family of labels anticipated for biological specimens in biology, will provide a practical approach to mapping of organelles and macromolecules in biological samples.

Materials and Methods

Sample Preparation

HeLa cells grown on MatTek dishes (MatTek corp) were transfected with MiniSOG-Rab5a. After 12 hours, cells were immediately fixed with 2% glutaraldehyde (EMS) in 0.1 M cacodylate buffer at pH 7.4 and photooxidation of MiniSOG (Shu, et al., 2011) was used to drive the deposition of compounds containing cerium or praseodymium. An adult male C57BL6 mouse was perfused, fixed and vibratomed with a Leica VT1000S, as previously described (Bushong, et al., 2002). Adjacent pairs of astrocytes in CA1 stratum radiatum were iontophoresed with fluorescent dyes. One astrocyte was iontophoresed with Lucifer Yellow and the other astrocyte with Neurobiotin-Alexa 568. The brain slices were further fixed with 4% paraformaldehyde (EMS) and 0.2% glutaraldehyde (EMS) in 1X PBS for 15 minutes. The brain slices were treated with the proprietary product containing either cerium or praseodymium, to be described elsewhere. Afterwards, the brain slices were fixed in 2% glutaraldehyde in 0.15M cacodylate buffer at pH 7.4 for 20 minutes and washed 5 times for 5 minutes each with buffer. Both cells and tissues were post-fixed with 1% osmium textroxide (EMS) in 0.15M cacodylate buffer at pH 7.4 for 30 minutes, dehydrated with an ethanol series and embedded in Durcupan ACM Fluka epoxy resin (Sigma) for both EELS and EFTEM. The embedded specimens were sectioned with a Leica Ultracut UCT ultramicrotome at 100–150 nm. The sections were glow discharged by a Cressington 208 Carbon Coater and a 1:5 dilution of 10 and 20 nm colloidal gold (Ted Pella) were added onto the sections. The sections were carbon coated by a Cressington 208 Carbon Coater on both sides of the sections to reduce section drift of sections under the beam and prevent the gold particles from coming of the sections.

Electron Microscopy

Electron microscopy was performed with a JEOL JEM-3200EF transmission electron microscope, equipped with a LaB_6 single crystal cathode operating at 300 KV. The microscope was fitted with an in-column Omega filter after the intermediate lenses and before the projector lenses. The spherical and chromatic aberration coefficients of the objective lens are 3.2 and 3.0 mm respectively. Conventional TEM and EFTEM images were collected using a condenser aperture of size 120 μm, an objective aperture of size 15 μm and entrance aperture of size 120 μm was used. Additionally, a selective area aperture of size 50 μm was used for acquisition of electron energy-loss spectra. The spectrometer energy resolution is 1.5 eV, measured as the FWHM of the zero loss peak. Before the acquisition of elemental maps, the region of interest was pre-irradiated with a low beam dose of 3.5×10^4 e$^-$/nm^2 for about 15 mins to stabilize the sample and to reduce contamination (Egerton, et al., 2004).

The recommended width of the energy filter to avoid blurring due to chromatic aberrations is between 10 – 50 eV (Hofer, et al., 1997). For our sample, the best compromise between resolution and SNR was obtained at an energy width of 40 eV. The elemental maps presented in this paper were obtained for cerium and praseodymium at their $M_{4,5}$ edge. The $M_{4,5}$ edge onset for Ce and Pr occurs at 883 and 931 eV respectively (Ahn & Krivanek, 1983). The elemental maps were constructed using the three-window method (Berger &

Kohl, 1993; Egerton, 1996) with two pre-edge images used to calculate and extrapolate the background signal, which is subsequently subtracted from the post-edge image acquired at the elemental edge. For accurate background subtraction, elemental maps constructed with a four-window method (3 pre-edges and 1 post-edge) are sometimes recommended (Heil, et al., 2012). We preferred a three-window method to a four-window method because the total acquisition time is less and hence, beam induced sample damage is significantly lower. For both Ce and Pr maps, the two pre-edge images were obtained at the same energy-loss region, of 791 – 831 eV and 836 – 876 eV, respectively. The post-edge image for Ce and Pr was obtained at an energy loss of 881 – 921 eV and 932 – 972 eV, respectively.

Image acquisition and processing

All of the images were acquired using two camera systems. One system is a DE-12 camera, which is a direct detection device from Direct Electron LP. (San Diego, CA). The other is a CCD based Ultrascan 4000 from Gatan (Pleasanton, CA). The format of the DE-12 detector is 3072×4096 pixels and the Ultrascan 4000 is a 4096×4096 pixel. The physical size of the pixels in the DE-12 detector and the Ultrascan 4000 are 6 μm and 15 μm respectively. The DE-12 detector is installed in the film chamber immediately below the viewing screen, and the Ultrascan 4000 is placed below the DE-12 detector. The geometric post-magnification was measured using the standard TEM calibration sample of diffraction grating replica from Ted Pella, and was found to be 1.2 and 1.7 for the DE-12 and Ultrascan 4000, respectively. The image acquisition and camera control of the Ultrascan 4000 was through the Digital Micrograph (Krivanek, et al.) image suite (Gatan Inc.) and the DE-12 was controlled by the micro-manager software (Edelstein, et al., 2010).

For both the pre and post edges, a series of sub-images were collected, each at 20 sec exposure per sub-image. The DE-12 is capable of reading out at 30 frames/second, however for this work, the frame rate was set to 0.1 frames/second (two frames are added to create a sub-image on the DE-12). The fast sub-frame, and rolling reset and readout makes much shorter sub-framing possible without any dead time during readout. Typically, for an image series obtained without any binning, a total of 16 sub-images were collected for each edge (exposure time = 320 sec per edge) with a total exposure time for all 3 edges of just under 16 mins. The sub-images in the series were merged into a single stack, and then aligned and summed to compensate for any specimen drift. The 10 and 15 nm gold nanoparticles dispersed on the sample were used to measure the successive drift between the sub-images in the stack. Initial attempts to measure drift between the sub-images using the cross-correlation algorithm of Digital Micrograph did not yield good results. The low SNR of the high-loss EFTEM images combined with presence of hot pixels either due to incorrect dark current subtraction or due to X-ray hits on the detector and fixed pattern artifacts, resulted in a spurious maximum intensity peak always occurring at the origin in the cross-correlated image (Shigematsu & Sigworth, 2013). We obtained consistent drift measurement values for image stacks acquired with both the Gatan Ultrascan and DE-12, using the MTrackJ plugin of ImageJ (Meijering, et al., 2012). The feasibility of more sophisticated drift correction algorithms have not been tested for our application (Schaffer, et al., 2004; Shigematsu & Sigworth, 2013). The positions of 3 gold nanoparticles were tracked for each sub-image of the stack, using the MTrackJ. A Gaussian smoothing filter of 3 pixels was applied to the

sub-images to improve the visibility of the nanoparticles. The average of X and Y drift vectors calculated from 2 of the 3 gold nanoparticles that showed lesser variance were used to calculate the drift vector. The sub-images were subsequently translated along the X and Y vectors to bring all the images of the stack in alignment. The aligned sub-images were then summed to give a corresponding pre or post edge image.

The resulting two pre-edges and the post-edge were then used to compute the elemental map by using the EELS analysis module of Digital Micrograph software (Gatan, Inc.). The background calculation was based on a power-law or constant R power law model of DM (Egerton, 1996; Gatan, 2012). The images from the DE-12 were imported into the Digital Micrograph software in order to perform the elemental mapping calculations. Since format of the pre-edge and post-edge images acquired on the DE-12 detector, were different from the format of the DM software acquisition, the image tags, which contain the spectrometer filter information and microscope imaging conditions had to be copied from a standard EFTEM image acquired with the DM software for the same imaging conditions, using a script (Mitchell, 2002). The EFTEM images acquired with the Gatan Ultrascan 4000 were dark current subtracted and flatfield corrected. The EFTEM images acquired with the DE-12 were dark current subtracted only. As described below, it is not necessary to perform gain normalization with a direct detection device.

Results and Discussions

In an effort to understand the extent to which the sample drifts during long acquisition times, we set out to measure drift on a standard sample. To measure the specimen drift, gold nanoparticles of size 10 and 20 nm were dispersed on a section of mouse brain and a thin layer of amorphous carbon was deposited on the sample to improve the sample stability under the electron beam (see Fig. 1a). The specimen was pre-irradiated under the electron beam at a low total dose of 3.7×10^4 e$^-$/nm^2 on the sample for about 10 mins. After beam stabilization, conventional TEM images were acquired at a magnification of 12000x for an exposure time of 1 sec, at an interval of every 2 min for an hour using the Ultrascan 4000 CCD detector. The sample was exposed to the electron beam continuously for the entire 1 hour, and for a total dose of 1.7×10^6 e$^-$/nm^2, which is typical of the dose the sample is subjected to during core-loss EFTEM imaging. The drift between successive images was calculated by the procedure described above. Fig. 1a shows the extent of the drift of 5 gold particles of 20 nm size between the first and last image. Fig. 1b shows the successive drift vectors in both X and Y directions. As can be seen in Fig. 1b, the sample drift is approximately along the same direction, however the magnitude of drift was not uniform varying from 1 pixel to 36 pixels between successive images. The net drift in X direction was 427 pixels (~ 7.2 pixels/min) and Y direction was 169 pixels (~ 2.8 pixels/min).

Fig. 2a shows a conventional TEM image with a 4k × 4k format of a cerium labeled endosome acquired with the Ultrascan 4000 at a screen magnification of 6kx for an exposure time of 1 sec. Fig. 2b shows an energy loss spectrum acquired on the Ce labeled endosome (darker regions) of Fig. 2a, obtained at a magnification of 10kx with a spectrum dispersion of 200 μm/eV and for an exposure time of 60 sec. In Fig. 2b, the presence of Ce can be seen clearly by its characteristic elemental M$_{4,5}$ edge onset at an energy-loss of 883 eV. Fig. 2c

shows a 4k × 4k Ce post-edge image of the region shown in Fig. 2a, obtained at screen magnification of 6kx with an exposure time of 20 sec on the Ultrascan 4000. Fig 2c clearly shows fixed pattern noise arising due to uncertainties in flat-fielding at low doses, which arise from variations in pixel dark noise, readout amplifier noise, as well as shot noise in the scintillator. Fig. 2d, shows a 3k × 4k Ce post edge image of the same region shown in Fig. 2c, acquired with a DE-12, at a screen magnification of 6kx and for an exposure time of 20 sec. The dose per pixel of the detector was kept the same as for the CCD image. The dose on the detector measured in conventional TEM mode was ~ 530 e⁻/pixel.sec, and was kept consistent for both the detectors during the energy-filtered image acquisition. It can be seen that the field of view is much smaller in Fig. 2d because the DE-12 is a much smaller detector (25 × 19 mm) in comparison to the Ultrascan 4000 detector (62 × 62 mm). The smaller physical size of pixels (6 μm) combined with the high modulation transfer function (MTF) of the DE-12, provides high spatial resolution and image detail even at lower screen magnifications (Jin, et al., 2008). Unfortunately, in the CCD systems, each electron incident on the scintillator screen will produce a footprint, that limits the spatial resolution of the CCD detectors. The FWHM of beam broadening for a 300 KV electron beam is about 30 μm for a bright self supported scintillator screen (Fan & Ellisman, 1993; Jin, et al., 2008). Additionally, for fiber coupled scintillator based cameras, as a result of backscattering from the underlying fiber-optic plate, the effective beam broadening can be as high as 50–100 μm (Daberkow, et al., 1991; Fan & Ellisman, 2000). The FWHM of the beam spread of a 300kV electron beam on a DDD detector calculated from the edge measurements was found to be ~ 12 μm, which is consistent with the specifications from the manufacturer (Direct Electron, 2013).

Fig. 2e and 2f, are magnified views of the summed Ce post-edge images of the region shown in a white box in Fig. 2c, acquired with the Ultrascan 4000 and the DE-12 detector, respectively. The summed images were created by adding 16 individual post-edge sub-images (shown in Fig. 2c and 2d) after they were corrected for any drift. Therefore, the effective exposure time for the images in Fig. 2e and 2f is 320 sec. Clearly, with the Ultrascan 4000, the fixed pattern noise in the individual sub-images (Fig. 2c) gets added up in the summed post-edge image in Fig. 2e. In addition to this, small white spots can be seen at the top left of Fig. 2e (region within the large white circle), also known as point blemishes, which are caused by spurious X-rays hitting the scintillator screen (Anderson, 2008). These are typically 1 – 4 pixels wide, and largely concentrated at the center of the detector (i.e. center of Fig. 2c), because X-rays travel in straight lines and their trajectories are not affected by the magnetic lenses of the TEM column. These point blemishes should not be confused with the somewhat larger bright spots seen in the image, which are due to the gold nanoparticles showing up in the background. In Comparison, the Ce post-edge obtained with the DE-12 detector looks clean, and has neither any fixed pattern noise nor point blemishes. The SNR was calculated for a ~ 50 nm × 50 nm region of the sample containing Ce particles for images in Fig. 2e and 2f. The SNR for the Ce post-edge acquired with the CCD based Ultrascan 4000 was 4.4, and the SNR for the Ce post-edge acquired with DE-12 detector was 12.5. This is a significant 2.8 times increase in SNR with the DE-12 detector.

In addition to increased SNR of the DE-12 detector in comparison with the CCD based Ultrascan 4000 detector, the total acquisition time is also considerably shorter. In case of the CCD detectors, the sensor remains exposed to the scintillator photons for the desired exposure time of the image, after which the charge accumulated in each pixel is readout sequentially into an output register and converted into a Digital Number by the A/D. Therefore, there is a dead time between readout of successive image, which is ~ 7 sec for a single 4k × 4k image. This increases the overall acquisition time by 35 % for the acquired image series on the Ultrascan 4000, which is consistent with > 50 % increase in the total acquisition time with CCD based detectors reported by other investigators (Heil & Kohl, 2010). The DE-12 sensor uses a massively parallel readout scheme, where the sensor is integrating charge for the next frame while reading out the previous frame. The dead time that the sensor is not responsive to primary electrons is well within 2 microsecond, negligible compared to the frame readout time of >25 milliseconds. The DE-12 sensor employs rolling shutter, which means that the beam shutter cannot be perfectly aligned with the start of the sensor readout. Therefore, the first frame of a sequential image series acquisition is discarded to remove the rolling shutter artifacts. This increases the overall acquisition time by just ~ 6% with the DE-12 detector.

Fig. 3a and 3b, show the calculated cerium elemental map of the region shown in Fig. 2, based on the use of the two cerium pre-edges and a cerium post edge (3-window method, power-law background subtraction), with Ultrascan 4000 and DE-12 detectors respectively. Fig. 3b, clearly shows the region where the cerium particles were tagged to the endosome, as expected. In Fig. 3a, it can be seen that the fixed pattern noise and the point blemishes seen in Fig. 2e are transferred to the cerium elemental map as well, and the locations of cerium particles in the image cannot be discerned from the background. Due to the fixed pattern noise, the cross-correlation between the 3 images (2 pre-edges and 1 post-edge) is extremely difficult, which is evident from the image artifact of alternating bright and dark spots (point blemishes) in Fig. 3a.

When the elemental maps are very noisy and contain artifacts, it is proposed that a better alternative may be the jump-ratio image (Hofer, et al., 1997; Krivanek, et al., 1993). The jump-ratio images are created by dividing the post-edge image by a pre-edge image (two window method), however, this is generally not used for elemental quantification as it is not considered a true elemental map (Hofer, et al., 1997). Fig 4a and 4b, show the jump-ratio image of the cerium labeled endosome shown in Fig. 2, based on the 1st pre-edge image (791 – 831 eV) and the post-edge image (881 – 921 eV), with the Ultrascan and the DE-12 detectors respectively. The cerium jump-ratio image obtained with the DE-12 detector (Fig. 4b) is comparable in contrast to the cerium elemental map obtained with the same detector (Fig. 3b). However, in case of the Ultrascan 4000 detector, the cerium jump ratio image (Fig. 4a) has better contrast than the cerium elemental map (Fig. 3a). Although, Fig. 4a is still noisy with the fixed pattern and point blemish artifacts, the cerium tagged endosome is visible in the image, which was otherwise completely lost in the noise in Fig. 3a.

The fixed pattern noise in the CCD images (see Fig. 2c, 2e, 3a and 4a) is due to uncertainties in flat-fielding, dark and read-out noise (Bosman & Keast, 2008; Howell, 2006; Shuman & Kruit, 1985). The flat-fielding process assumes that the pixels are uniformly illuminated,

however this is not true for core-loss EFTEM imaging as the total dose on the detector is extremely low and the relative intensity variations resulting from large variations in the number of photons produced by each electron in the phosphor for such low electron fluxes between adjacent pixels can be extremely large. The DE-12 detector detects electrons directly, and is not subjected to the discrepancies arising from electron to photon conversion. The direct detector images are of course subject to fluctuations in the number of electron-hole pairs produced by a primary electron interaction in the epitaxial layer. However, pixel-to-pixel variations in gain are not as significant a problem with the DDD detector. The result is that EFTEM images can be obtained with just the dark current subtracted on the DE-12 detector without the appearance of fixed pattern artifacts.

The signal to noise in pre/post edge images obtained with the CCD detector can be minimized, by performing an on-chip pixel binning. For example, a 4×4 pixel binning operation would result in a final signal value that is 16 times that of a single pixel value, but only 1 times the read noise. Fig. 5a shows a conventional TEM image, at $4k \times 4k$ format, of a praseodymium labeled astrocyte acquired on the Ultrascan 4000 at a screen magnification of 6kx, for an exposure time of 1 sec. Fig. 5b shows an energy loss spectrum acquired on the Pr regions of Fig. 5a, obtained at a magnification of 20kx, for a spectrum dispersion of 150 μm/eV and for an exposure time of 20 sec. In Fig. 5b, the presence of Pr can be seen clearly by its characteristic elemental $M_{4,5}$ edge onset at an energy-loss of 931 eV. Fig. 5c shows a $1k \times 1k$ summed Pr post-edge image, acquired with the Ultrascan 4000, for a 4×4 hardware binning. The summed image in Fig. 5c was created by adding 8 individual Pr post-edge sub-images, each acquired for 20 sec exposure. Clearly, binning has eliminated the fixed pattern noise seen in Fig. 2c, but with a proportional decrease in the image resolution. Fig. 5d shows a $3k \times 4k$ summed Pr post-edge image acquired with the DE-12 detector, without any binning and hence retaining the full native resolution of microscope-detector system. Fig. 5d was created by adding 10 individual Pr post-edge sub-images on the DE-12, each acquired for 20 sec exposure. The SNR for the binned Ultrascan 4000 in Fig. 5c is 8.0 and nearly the same as the SNR for the unbinned DE-12 image in Fig. 5d, which is 8.2. The SNR was calculated for a ~ 120 nm × 120 nm region of the sample containing Pr particles for images in Fig. 5c and 5d.

The dose on the detector measured in conventional TEM mode prior to any binning was ~ 470 e⁻/pixel.sec, and was kept consistent for both the detectors during the energy-filtered image acquisition. To obtain the same SNR, the CCD Ultrascan 4000 was exposed ~ 12.8 times the dose of the DE-12 detector. Fig. 5e and 5f, are the Pr maps obtained by the 3-window method (constant R power-law subtraction) with the Ultrascan 4000 and DE-12 respectively. With binning, an elemental map of reasonable quality can be obtained on the Ultrascan 4000, which was otherwise very difficult to obtain without binning (see Fig. 3a). However, the image detail of the CCD elemental map (Fig. 5e) is inferior to DE-12 elemental map (Fig. 5f).

Conclusion

To compensate for the sample drift during the long exposures required for core-loss energy-filtered TEM imaging, sub-images were acquired at shorter exposure times and then

subsequently aligned and summed. We have shown that with the use of the DE-12 direct detection device (DDD), a 3x improvement in SNR in comparison to the Gatan Ultrascan 4000 charge coupled device (CCD) for the acquisition of energy-filtered TEM images in the core-loss region. As the Ultrascan 4000 is a high-end fiber-coupled CCD based system, we expect these results to be accurate in comparison with CCD based systems in general. The improvements in SNR with DDD are dramatic. We expect further improvements with the use of the latest back-thinned DDD detectors. Also, due to the zero dead time between readouts, the DDD detectors should enable interesting applications in the low-loss region, as in the case of real time in-situ elemental imaging.

Acknowledgments

References

Ahn, CC.; Krivanek, OL. EELS Atlas. Gatan; 1983.

Anderson IM. Statistical and Systematic Errors in EFTEM Spectral Imaging. Microsc Microanal. 2008; 14(Suppl 2):2008. http://www.nist.gov/mml/mmsd/837-802-anderson-2008-medianfilter.cfm.

Aoyama K, Matsumoto R, Komatsu Y. How to make mapping images of biological specimens - data collection and image processing. J Electron Microsc. 2002; 51(4):257–263.

Aronova MA, Kim YC, Harmon R, Sousa AA, Zhang G, Leapman RD. Three-dimensional elemental mapping of phosphorus by quantitative electron spectroscopic tomography (QuEST) (Reprinted from J. Struct. Biol, vol 160, pg 35–48, 2007). J Struct Biol. 2008; 161(3):322–335. [PubMed: 18342742]

Aronova MA, Kim YC, Pivovarova NB, Andrews SB, Leapman RD. Quantitative EFTEM mapping of near physiological calcium concentrations in biological specimens. Ultramicroscopy. 2009; 109(3): 201–212. [PubMed: 19118952]

Berger A, Kohl H. Optimum Imaging Parameters for Elemental Mapping in an Energy Filtering Transmission Electron-Microscope. Optik. 1993; 92(4):175–193.

Bosman M, Keast VJ. Optimizing EELS acquisition. Ultramicroscopy. 2008; 108(9):837–846. [PubMed: 18375066]

Browning ND, Wallis DJ, Nellist PD, Pennycook SJ. EELS in the STEM: Determination of materials properties on the atomic scale. Micron. 1997; 28(5):333–348.

Bushong EA, Martone ME, Jones YZ, Ellisman MH. Protoplasmic astrocytes in CA1 stratum radiatum occupy separate anatomical domains. J Neurosci. 2002; 22(1):183–192. [PubMed: 11756501]

Carter, CB.; Williams, DB. Transmission Electron Microscopy. Springer; 2009.

Daberkow I, Herrmann KH, Liu LB, Rau WD. Performance of Electron Image Converters with Yag Single-Crystal Screen and Ccd Sensor. Ultramicroscopy. 1991; 38(3–4):215–223.

Direct Electron, I. Features of DE-12 Camera System. 2013. http://www.directelectron.com/cameras/de/overview/

Edelstein, A.; Amodaj, N.; Hoover, K.; Vale, R.; Stuurman, N. Computer Control of Microscopes Using Manager. John Wiley & Sons, Inc; 2010.

Egerton RF. Parallel-Recording Systems for Electron-Energy Loss Spectroscopy (EELS). J Electron Micr Tech. 1984; 1(1):37–52.

Egerton, RF. Electron Energy-Loss Spectroscopy. Plenum Press; 1996.

Egerton RF, Li P, Malac M. Radiation damage in the TEM and SEM. Micron. 2004; 35(6):399–409. [PubMed: 15120123]

Fan GY, Ellisman MH. High-Sensitivity Lens-Coupled Slow-Scan Ccd Camera for Transmission Electron-Microscopy. Ultramicroscopy. 1993; 52(1):21–29. [PubMed: 8266607]

Fan GY, Ellisman MH. Digital imaging in transmission electron microscopy. J Microsc-Oxford. 2000; 200:1–13.

Gatan, I. Gatan EELS Analysis. 2012. http://www.gatan.com/files/PDF/Product_Manuals/ EELS_Analysis_User_Guide.pdf

Grogger W, Varela M, Ristau R, Schaffer B, Hofer F, Krishnan KM. Energy-filtering transmission electron microscopy on the nanometer length scale. J Electron Spectrosc. 2005; 143(2–3):139– 147.

Heil T, Gralla B, Epping M, Kohl H. Improving the reliability of the background extrapolation in transmission electron microscopy elemental maps by using three pre-edge windows. Ultramicroscopy. 2012; 118:11–16. [PubMed: 22728399]

Heil T, Kohl H. Optimization of EFTEM image acquisition by using elastically filtered images for drift correction. Ultramicroscopy. 2010; 110(7):745–750.

Hofer F, Grogger W, Kothleitner G, Warbichler P. Quantitative analysis of EFTEM elemental distribution images. Ultramicroscopy. 1997; 67(1–4):83–103.

Howell, SB. Handbook of CCD Astronomy. Cambridge University Press; 2006.

Hunt JA, Williams DB. Electron Energy-Loss Spectrum-Imaging. Ultramicroscopy. 1991; 38(1):47– 73.

Jin L, Milazzo AC, Kleinfelder S, Li SD, Leblanc P, Duttweiler F, Bouwer JC, Peltier ST, Ellisman MH, Xuong NH. Applications of direct detection device in transmission electron microscopy. J Struct Biol. 2008; 161(3):352–358. [PubMed: 18054249]

Krivanek, O.; Gubbens, A.; Kundmann, M.; Carpenter, G. PROCEEDINGS OF THE ANNUAL MEETING-ELECTRON MICROSCOPY SOCIETY OF AMERICA. SAN FRANCISCO PRESS; Elemental mapping with an energy-selecting imaging filter; p. 586-586.

Leapman RD. Detecting single atoms of calcium and iron in biological structures by electron energy-loss spectrum-imaging. J Microsc-Oxford. 2003; 210:5–15.

Leapman RD, Aronova MA. Localizing specific elements bound to macromolecules by EFTEM. Method Cell Biol. 2007; 79:593–613.

Lozano-Perez S, Bernal VD, Nicholls RJ. Achieving sub-nanometre particle mapping with energy-filtered TEM. Ultramicroscopy. 2009; 109(10):1217–1228. [PubMed: 19505762]

Meijering E, Dzyubachyk O, Smal I. Methods for Cell and Particle Tracking. Method Enzymol. 2012; 504:183–200.

Milazzo AC, Lanman J, Bouwer JC, Jin L, Peltier ST, Johnson JE, Kleinfelder S, Xuong NH, Ellisman MH. Advanced Detector Development for Electron Microscopy Enables New Insight into the Study of the Virus Life Cycle in Cells and Alzheimer's Disease. Microsc Microanal. 2009; 15:8–9.

Milazzo AC, Leblanc P, Duttweiler F, Jin L, Bouwer JC, Peltier S, Ellisman M, Bieser F, Matis HS, Wieman H, Denes P, Kleinfelder S, Xuong NH. Active pixel sensor array as a detector for electron microscopy. Ultramicroscopy. 2005; 104(2):152–159. [PubMed: 15890445]

Milazzo AC, Moldovan G, Lanman J, Jin LA, Bouwer JC, Klienfelder S, Peltier ST, Ellisman MH, Kirkland AI, Xuong NH. Characterization of a direct detection device imaging camera for transmission electron microscopy. Ultramicroscopy. 2010; 110(7):741–744. [PubMed: 20189305]

Mitchell, D. Dave Mitchell Digital Micrograph Scripting Website. 2002. http://www.dmscripting.com/ copy_all_tags_between_images.html

Schaffer B, Grogger W, Kothleitner G. Automated spatial drift correction for EFTEM image series. Ultramicroscopy. 2004; 102(1):27–36. [PubMed: 15556698]

Shigematsu H, Sigworth FJ. Noise models and cryo-EM drift correction with a direct-electron camera. Ultramicroscopy. 2013; 131:61–69. [PubMed: 23748163]

Shu XK, Lev-Ram V, Deerinck TJ, Qi YC, Ramko EB, Davidson MW, Jin YS, Ellisman MH, Tsien RY. A Genetically Encoded Tag for Correlated Light and Electron Microscopy of Intact Cells, Tissues, and Organisms. Plos Biol. 2011; 9(4)

Shuman H, Kruit P. Quantitative Data-Processing of Parallel Recorded Electron Energy-Loss Spectra with Low Signal to Background. Rev Sci Instrum. 1985; 56(2):231–239.

Suenaga K, Sato Y, Liu Z, Kataura H, Okazaki T, Kimoto K, Sawada H, Sasaki T, Omoto K, Tomita T, Kaneyama T, Kondo Y. Visualizing and identifying single atoms using electron energy-loss spectroscopy with low accelerating voltage. Nat Chem. 2009; 1(5):415–418. [PubMed: 21378897]

Terada S, Aoyama T, Yano F, Mitsui Y. Time-resolved acquisition technique for elemental mapping by energy-filtering TEM. J Electron Microsc. 2001; 50(2):83–87.

Xuong NH, Jin L, Kleinfelder S, Li SD, Leblanc P, Duttweiler F, Bouwer JC, Peltier ST, Milazzo AC, Ellisman M. Future directions for camera systems in electron microscopy. Method Cell Biol. 2007; 79:721–739.

Xuong NH, Milazzo AC, Leblanc P, Duttweiler F, Bouwer JC, Peltier ST, Ellisman M, Denes P, Bieser F, Matis HS. First use of a high-sensitivity active pixel sensor array as a detector fpr electron microscopy. Proc SPIE. 2004; 5301:242.

Zhang PJ, Land W, Lee S, Juliani J, Lefman J, Smith SR, Germain D, Kessel M, Leapman R, Rouault TA, Subramaniam S. Electron tomography of degenerating neurons in mice with abnormal regulation of iron metabolism. J Struct Biol. 2005; 150(2):144–153. [PubMed: 15866737]
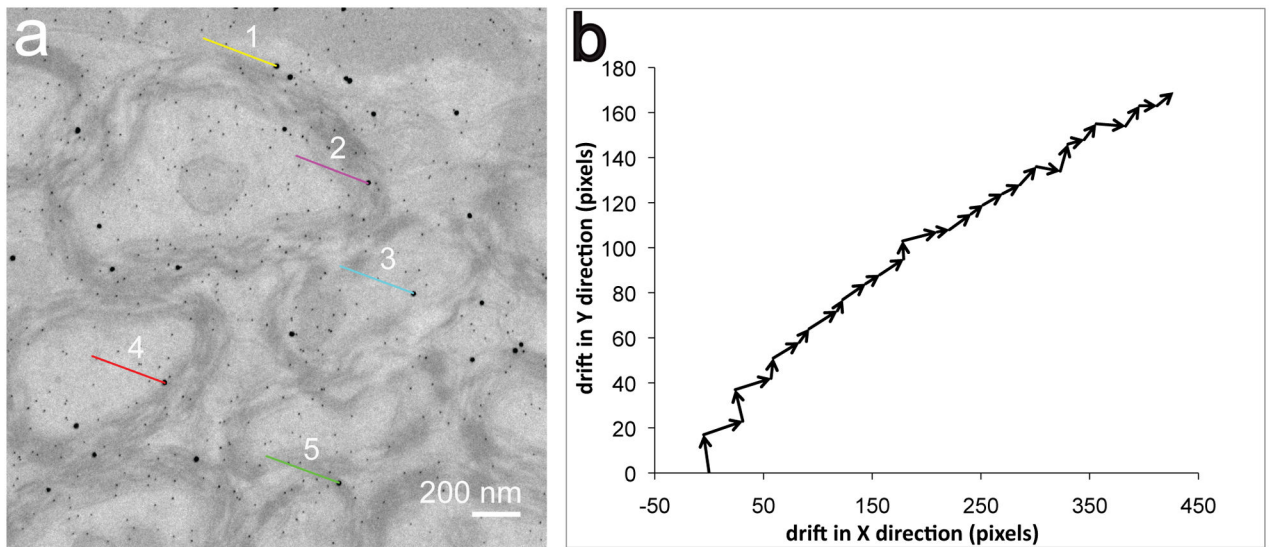
Figure 1.
(a) Shows the direction and the extent of drift (see the marked lines in the image) for 5 randomly chosen gold nanoparticles dispersed on a section of myelinated axons at corpus callosum, after 1 hr. The drift was calculated by acquiring a series of 30 conventional TEM images (4k × 4k) at an interval of 2 min for an exposure of 1 sec. (b) Shows the drift vector between successive images; an average drift of 7.2 pixels/min in the X direction and 2.8 pixels/min in the Y direction was observed.
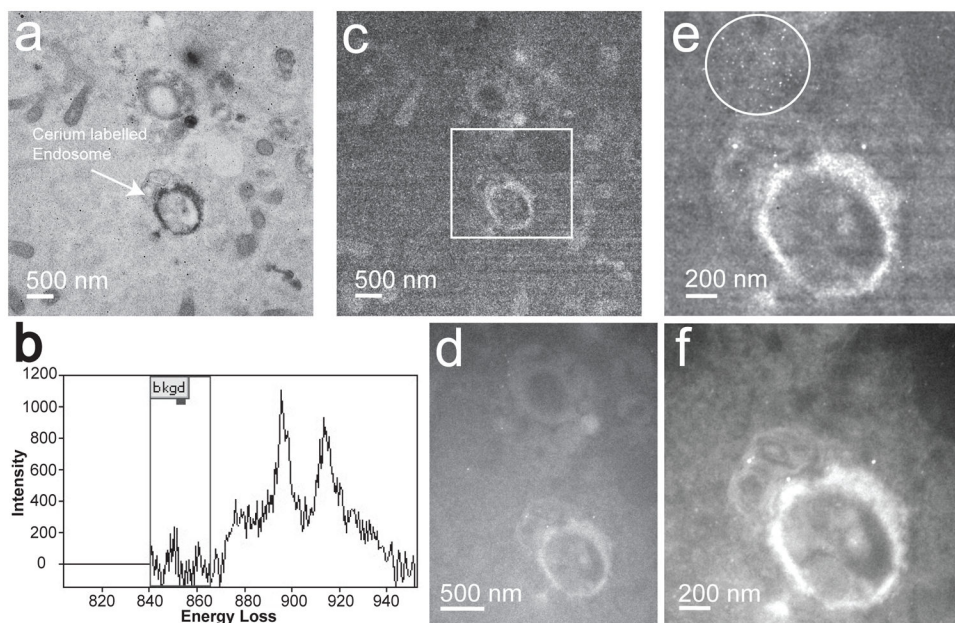
Figure 2.
(a) A conventional TEM image (4k × 4k) of Ce labeled endosome, acquired by an Ultrascan 4000 at a screen magnification of 6kx and exposure time of 1 sec. The darker regions show presence of Ce particles. (b) An energy-loss spectra obtained for a 60 sec exposure, showing the onset of Ce edge at 883 eV. (c) Shows a Ce post-edge image (4k × 4k) acquired at viewing screen magnification of 6kx and exposure time of 20 sec on the Ultrascan 4000 for a 40 eV slit width. (d) Shows a Ce post-edge image (4k × 3k) also acquired viewing screen magnification of 6kx, and for the same imaging conditions as in (c) with the DE-12 detector. (e) Summed Ce post-edge images (4k × 4k) obtained after adding 16 drift corrected individual post-edge images acquired on the Ultrascan 4000. (f) Summed Ce post-edge images (3k × 4k) obtained after adding 16 drift corrected individual post-edge images acquired on the DE-12. (e) and (f) are the magnified view of the region shown in a white box in (c). The large white circle in (e) shows the region affected by point blemishes caused by spurious X-rays hitting the detector. The Gaussian smoothing filter of 3 pixels was applied to figures (c) – (f).
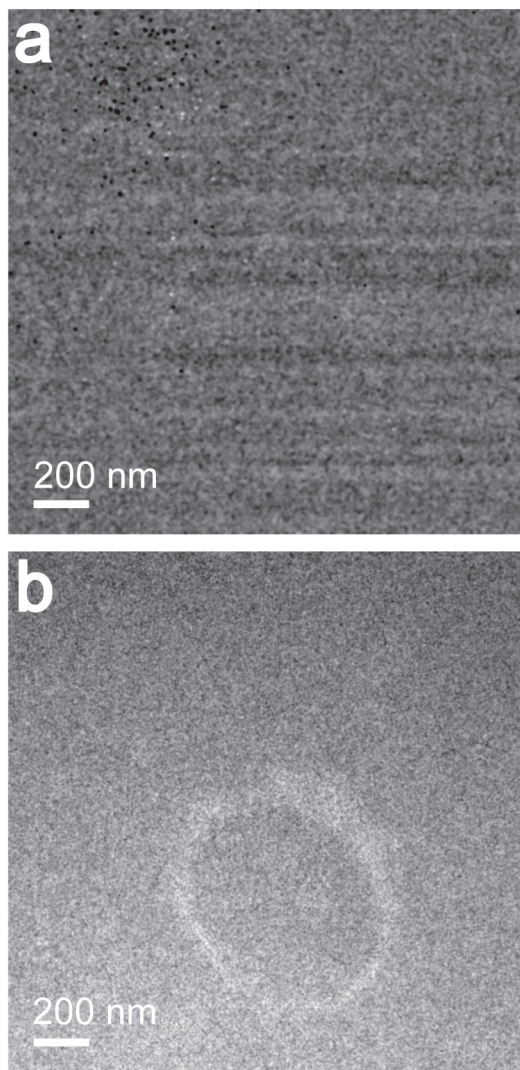
Figure 3.
(a) Shows a cerium elemental map from the region shown in Fig. 2, obtained using an Ultrascan 4000. (b) Shows a cerium map obtained from the same region using a DE-12 detector. The Gaussian smoothing filter of 3 pixels was applied to the images.
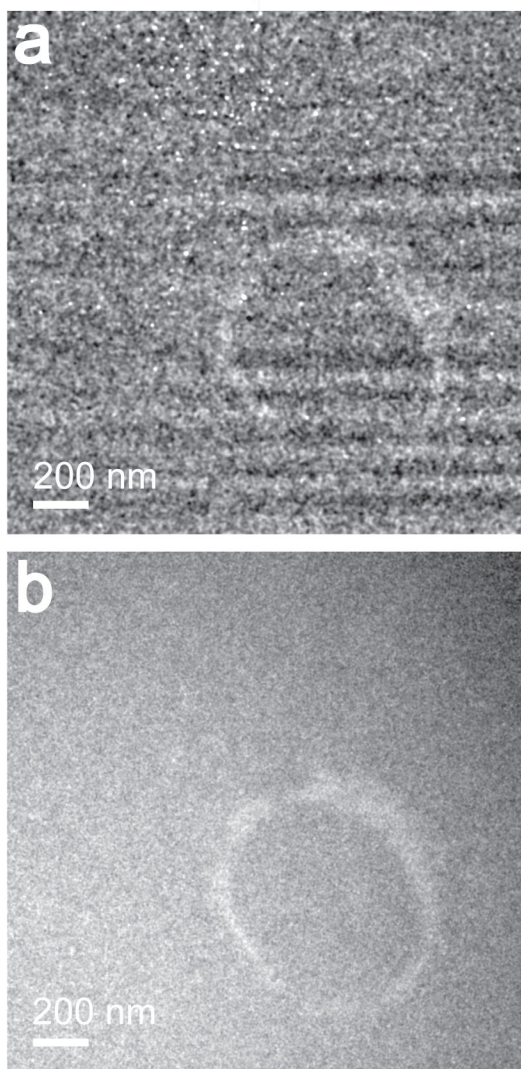
Figure 4.
Shows a cerium jump-ratio image using the 1st pre-edge (791 – 831 eV) and the post-edge (881 – 921 eV) image from the region shown in Fig. 2. (a) using an Ultrascan 4000 detector. (b) using a DE-12 detector. The Gaussian smoothing filter of 3 pixels was applied to the images.
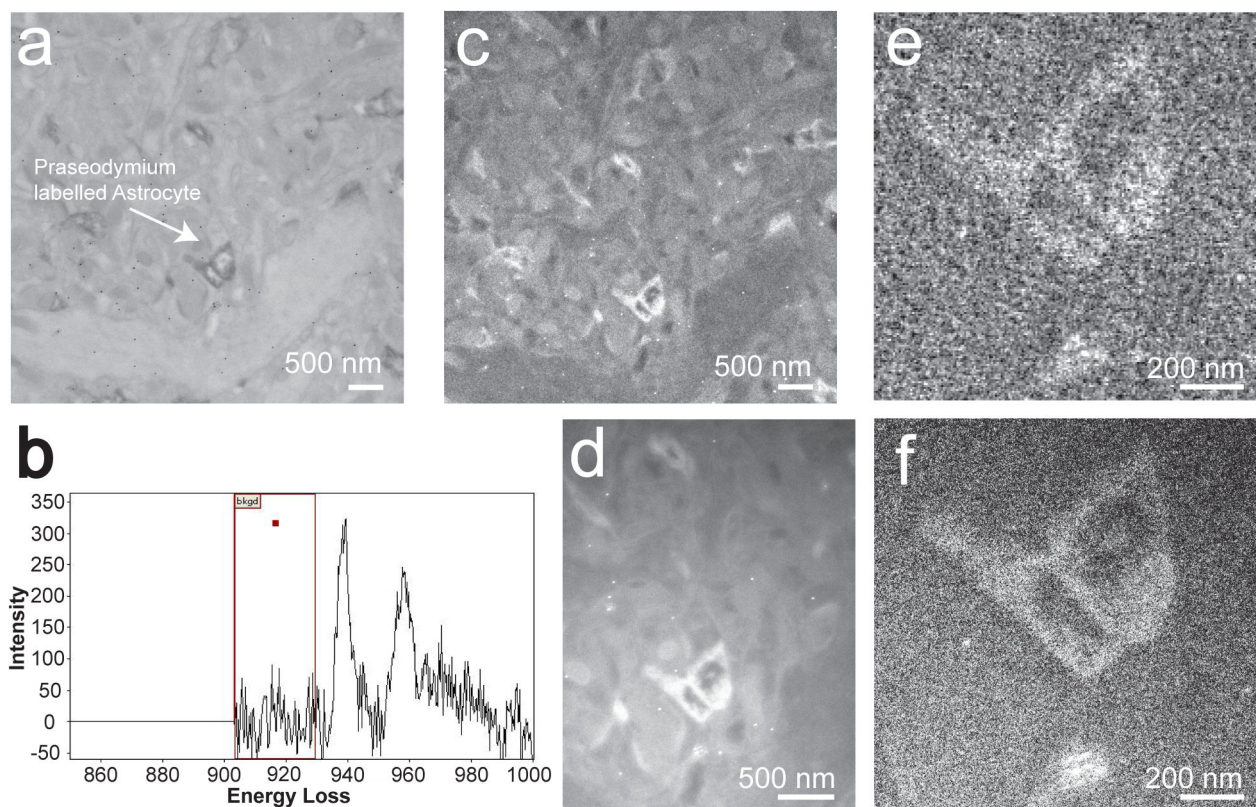
Figure 5.
(a) A conventional TEM image (4k × 4k) of Pr labeled astrocyte, acquired with an Ultrascan 4000 at a screen magnification of 10kx and exposure time of 1 sec. The regions of darker contrast show presence of Pr particles. (b) An energy-loss spectra obtained for a 20 sec exposure, showing the onset of Pr edge at 931 eV. (c) Shows a 1k × 1k summed Pr post-edge image of 8 individual drift corrected images, each acquired for a 20 sec exposure by an Ultrascan 4000. An on-chip hardware binning of 4 × 4 pixels was used. (d) Shows a 3k × 4k summed Pr post-edge image of 10 individual drift corrected images, each acquired for a 20 sec exposure with the DE-12, without any binning. (e) Pr map for the images acquired by an Ultrascan 4000. (f) Pr map for the images acquired by a DE-12.